Research Article

# Using Soft Polymer Template Engineering of Mesoporous TiO₂ Scaffolds to Increase Perovskite Grain Size and Solar Cell Efficiency

Qing Lian,* Muhamad Z. Mokhtar, Dongdong Lu, Mingning Zhu, Janet Jacobs, Andrew B. Foster, Andrew G. Thomas, Ben F. Spencer, Shanglin Wu, Chen Liu, Nigel W. Hodson, Benjamin Smith, Abdulaziz Alkaltham, Osama M. Alkhudhari, Trystan Watson, and Brian R. Saunders*

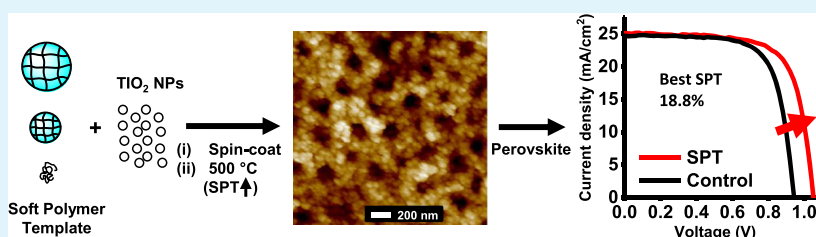Cite This: ACS Appl. Mater. Interfaces 2020, 12, 18578−18589

Read Online

ACCESS | 📊 Metrics & More | 📰 Article Recommendations | SI Supporting Information

**ABSTRACT:** The mesoporous (meso)-TiO₂ layer is a key component of high-efficiency perovskite solar cells (PSCs). Herein, pore size controllable meso-TiO₂ layers are prepared using spin coating of commercial TiO₂ nanoparticle (NP) paste with added soft polymer templates (SPT) followed by removal of the SPT at 500 °C. The SPTs consist of swollen crosslinked polymer colloids (microgels, MGs) or a commercial linear polymer (denoted as LIN). The MGs and LIN were comprised of the same polymer, which was poly(N-isopropylacrylamide) (PNIPAm). Large (L-MG) and small (S-MG) MG SPTs were employed to study the effect of the template size. The SPT approach enabled pore size engineering in one deposition step. The SPT/TiO₂ nanoparticle films had pore sizes > 100 nm, whereas the average pore size was 37 nm for the control meso-TiO₂ scaffold. The largest pore sizes were obtained using L-MG. SPT engineering increased the perovskite grain size in the same order as the SPT sizes: LIN < S-MG < L-MG and these grain sizes were larger than those obtained using the control. The power conversion efficiencies (PCEs) of the SPT/TiO₂ devices were ~20% higher than that for the control meso-TiO₂ device and the PCE of the champion S-MG device was 18.8%. The PCE improvement is due to the increased grain size and more effective light harvesting of the SPT devices. The increased grain size was also responsible for the improved stability of the SPT/TiO₂ devices. The SPT method used here is simple, scalable, and versatile and should also apply to other PSCs.

## INTRODUCTION

The power conversion efficiency (PCE) of perovskite solar cells (PSC) has increased from 3.8% in 2009[1] to 25.2%,[2] which is exceptional. Many high-efficiency PSCs use a mesoporous (meso-) TiO₂ layer,[1,3−7] which evolved from dye-sensitized solar cells. The electron transport within the meso-TiO₂ layer has been enhanced by doping Li, Ta, and Nb[8−11] into the TiO₂ layer. The PCE of PSCs and other solar cells[12] has been increased through pore size engineering of meso-TiO₂.[13−15] A seminal study by Hwang et al. used polystyrene (PS) particles as templates to include well-controlled pores within meso-TiO₂ layers for PSCs.[13] However, the PS particles were hard spheres in the solvent used to deposit the TiO₂ nanoparticles (NPs), which brings into question the important issue of template colloidal stability during film formation. Shao et al. added a linear polymer into TiO₂ paste to increase the pore size of the printed TiO₂ layer for PSCs.[14] Their polymer system was not particulate and

should have dissolved well in the solvent used to deposit the TiO₂ NPs. Indeed, their PCE values were relatively high. Their system contained multiple components and home-made TiO₂ nanoparticles (NPs), which may render adoption of that approach challenging. In contrast, we aimed to use a polymer that was in the soft (swollen) state and as many commercial ingredients as possible to provide a simple and versatile templating method for improving the control of meso-TiO₂ pore size using pore size engineering. We hypothesized that increasing the meso-TiO₂ pore size would increase perovskite (PVK) grain size and PCE.
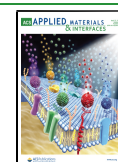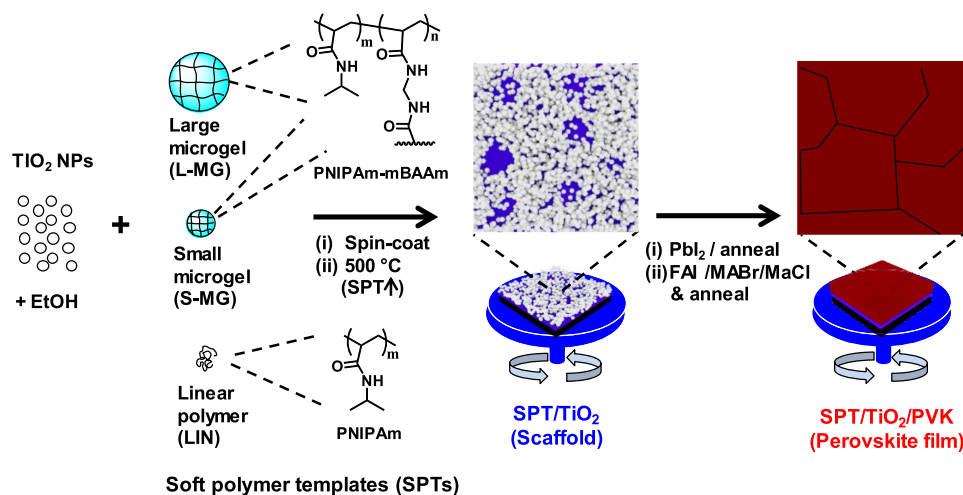
**Figure 1.** Preparation of soft polymer-templated (SPT)/TiO$_2$ and SPT/TiO$_2$/perovskite (PVK) films. The PNIPAm MG particles are crosslinked by mBAAm and swell in the solvent (EtOH, ethanol). LIN (i.e., linear PNIPAm) chains were not crosslinked and are swollen coils in EtOH. These SPTs form pores within the TiO$_2$ nanoparticle (NP) layer during spin coating and are subsequently removed by high-temperature sintering.

The regular n−i−p architecture has been widely used for fabricating PSCs[16] and consists of glass/indium tin oxide (ITO) (or fluorine-doped tin oxide, FTO)/electron-transport layer/perovskite layer/hole-transport layer/metal electrode. Compared with a planar architecture, PSCs with a meso-TiO$_2$ layer generally show a higher efficiency[17−22] and lower hysteresis.[17,18,22,23] This is because a larger interfacial area between TiO$_2$ and the perovskite in the mesoporous structure leads to faster electron transport. The extent of infiltration of the perovskite within the meso-TiO$_2$ layer strongly affects the PCE and this has led researchers to engineer the porosity. Xiao et al. used nanoporous TiO$_2$ spheres to prepare PSCs.[24] Ramos et al. constructed one-dimensional (1D) TiO$_2$ nanocolumnar electron-transport layers (ETLs) to give viable PSCs.[25] Chen et al. used three-dimensional (3D) rutile TiO$_2$ nanodendrite arrays for their PSCs. Granados et al. mixed poly-(vinylpyrrolidone) (PVP) within the TiO$_2$ layer and achieved pore sizes of 15−30 nm.[26] Hörantner et al. used PS spheres to increase the pore size of TiO$_2$.[27] However, the above methods could not be performed in one step or only gave modest PCE values. None of these approaches used templating species that were colloidally stable when mixed with dispersed TiO$_2$ nanoparticles (NPs). However, colloidal stability is essential to achieve well-distributed template particles. What is missing from the literature is a simple method that enables pores greater than 100 nm in size to be prepared through one-step TiO$_2$ NP/template deposition. Here, we introduce such an approach to engineer pores greater than 100 nm in templated meso-TiO$_2$ films and use these films to provide high PCE PSCs. We denote this approach as a soft polymer template (SPT) pore size engineering because the polymers employed are in the soft (swollen) state at the point where the TiO$_2$ NP scaffold is deposited.

The new pore size engineering approach presented in this study is very different from additive engineering, which has been widely studied for PSCs.[28,29] The former involves using a removable template to adjust the size of the pores within the meso-TiO$_2$ scaffold. Additive engineering involves addition of small molecules, polymers,[30] surfactants, or quantum dots[29] to the precursor perovskite (PVK) solution[31,32] or PVK interfaces.[29] These additives usually directly interact with PbI$_2$ or PVK, control crystallization or provide passivation, and remain within (or at the surface of) the PVK grains. For example, Zuo et al. studied polymer-modified PVKs and used poly(4-vinylpyridine) to form coordination bonds with PVK crystals during crystallization.[30] In contrast, we use our SPT additives as pore size templates for the meso-TiO$_2$ scaffold and remove them before the PVK precursor solution is added. Hence, there is no interaction between the SPT and PVK.

Two of the SPTs used in this study are microgels (MGs). MGs are crosslinked polymer colloids that swell in a good solvent.[33,34] MGs have excellent colloidal stability and film-forming properties.[34] Our group has used hydrophobic PS MGs in the hole-transport matrix of PSCs[35] as well hydrophilic poly(N-vinylformamide) (PNVF) MGs as additives for the perovskite photoactive layer.[36] We postulated that the swollen nature of MGs would give a potentially useful additive for pore formation in the meso-TiO$_2$ layer. Unfortunately, neither PS MGs or PNVF MGs swell in ethanol (EtOH), the solvent used for TiO$_2$ paste, which prevented colloidal stability being achieved. However, EtOH is a thermodynamically good solvent for PNIPAm.[37] Therefore, poly(N-isopropylacryla-mide) (PNIPAm) was selected to construct our SPT MG particles. It is the combination of the amide and isopropyl groups within PNIPAm that enabled the polymer to swell in EtOH. We stress that this study is the first time that (i) MGs have been used to adjust the pore size of meso-TiO$_2$ films and (ii) MG template meso-TiO$_2$ films have been used to construct PSCs. Furthermore, in contrast to our earlier studies where MGs were used as additives,[35,36] here the MGs are removed (burnt out) by heating to 500 °C and do not remain in the PSCs. The method used to prepare the SPT/TiO$_2$ films and perovskite films (SPT/TiO$_2$/PVK) is depicted in Figure 1. The PCEs of the present devices are 2−3 times higher than those obtained for the earlier PSCs that contained MGs.[35,36] Figure S1 summarizes the previous PSC studies using MGs as well as the PCEs and confirms the novelty of the present work.

The first aim of this study was to increase the pore size of meso-TiO$_2$ using one-step deposition. Two MG systems with different sizes (large, L-MG and small, S-MG) and linear PNIPAm (LIN) are used for this purpose (Figure 1). The MGs can be prepared at the multiton scale in principle. We employed commercial TiO$_2$ paste, which contains EtOH, and synthesized MGs and purchased LIN. The study begins with a

characterization of the MGs and LIN followed by an investigation of SPT/TiO$_2$ NP film morphology. We then prepare SPT/TiO$_2$/PVK films and show that the grain size increased compared to control films. The SPT/TiO$_2$/PVK PSCs are shown to have much higher PCEs (champion PCE of 18.8%) than the control system. The high PCE of the LIN/TiO$_2$/PVK PSC (17.2%) demonstrates the versatility of our approach because this system was constructed using commercial materials. The SPT approach should be applicable to other PSCs that employ meso-TiO$_2$ scaffolds.

## ■ EXPERIMENTAL SECTION

**Materials.** Linear poly(N-isopropylacrylamide) (PNIPAm denoted as LIN, average $M_n$ = 85 000 g/mol, Sigma product number 901422), ammonium persulfate (APS, ≥98.0, Sigma), NIPAm (≥99%), N,N′-methylene bis(acrylamide) (mBAAm, 99%, Sigma), potassium persulfate (KPS, 99%, Sigma), methacrylic acid (MAA, Sigma, 98%), sodium dodecyl sulfate (SDS, 98.5%, Sigma), methylammonium bromide (MABr, ≥99.5%, Ossila), methylammonium chloride (MACl), formamidinium Iodide (FAI, 98%, Ossila), and PbI$_2$ (99.99% trace metals basis, TCI) were all used as received. N,N-dimethylformamide (DMF, 99.8%, Acros), dimethyl sulfoxide (DMSO, ≥99.7%, Acros), TiO$_2$ paste (18 NRT, 19 wt %, GreatCell Solar), titanium diisopropoxide bis(acetylacetonate) (TAA, 75 wt % in isopropanol, Sigma), titanium isopropoxide (TIP, 97%, Sigma), spiro-MeOTAD (Spiro, 99%, Sigma), and 4-tert-butylpyridine (TBP, 96%, Sigma) were all used as received. Bis(trifluoromethane)-sulfonimide lithium salt (Li-TFSI, 99.95%, Sigma), tris(2-(1H-pyrazol-1-yl)-4-tert-butylpyridine) cobalt(III) tri[bis-(trifluoromethane) sulfonimide] (FK209 Co(III) TFSI), acetonitrile (>99.9%, Acros), 1-butanol (BuOH, anhydrous, 99.8%, Sigma), chlorobenzene (CBZ, 99.8%, Acros), acetone (ACS reagent, ≥99.5%, Fisher Scientific), absolute ethanol (EtOH, >99.8%, Fisher Scientific), and 2-propanol (IPA, 99.5%, Acros) were also used as received. All water used was of ultra-high-purity quality.

**Synthesis of Small Microgels.** The S-MG particles were prepared by precipitation polymerization following a reported method.[38] Briefly, NIPAm (1.50 g, 13.2 mmol), mBAAm (20.6 mg, 0.13 mmol), and SDS (40 mg) were added to water (100.0 mL). The solution was degassed with N$_2$ gas for 1 h in a 250 mL glass reactor equipped with a stirrer and the solution was heated to 70 °C. Then, APS (65 mg) dissolved in water (0.30 mL) was quickly added to start the polymerization and stirring was maintained. The reaction mixture was stirred for 4 h under a nitrogen atmosphere and cooled to room temperature. The dispersion was then dialyzed against EtOH for 6 weeks with regular solvent changes to replace the dispersion medium with EtOH.

**Synthesis of Large Microgels.** The L-MG particles were prepared by precipitation polymerization based on the work of Zhan et al.[39] Briefly, NIPAm (188 mg, 1.62 mmol), mBAAm (3.0 mg, 0.019 mmol), MAA (16.2 mg, 0.18 mmol), and SDS (5.4 mg) were dissolved in water (20.0 mL). This mixture was then degassed with N$_2$ for 1 h at 70 °C in a 50 mL glass reactor equipped with a stirrer. To begin particle growth, KPS aqueous solution (5.0 mL, 10 mM) was quickly added. The polymerization was conducted at 70 °C for ∼7 h under a N$_2$ atmosphere. The aqueous dispersion medium was replaced using five centrifugation (at 1180 g)/resuspension cycles in EtOH.

**Mesoporous TiO$_2$ Film Preparation.** For the preparation of the control meso-TiO$_2$ film, 18 NRT paste (1.0 g, 19 wt %) was diluted to 9.9 mL with EtOH to give a TiO$_2$ concentration of 19.0 mg/mL. Then, the TAA solution (80 μL) was added to give a concentration of 6.0 mmol. Control TiO$_2$ films were made by dropping a portion of the TiO$_2$ dispersion (80 μL) onto ITO glass and then spin coating at 2000 rpm for 30 s. Finally, the substrate was transferred into a preheated furnace and sintered at 500 °C for 30 min.

**Linear PNIPAm/TiO$_2$ Film Preparation.** TiO$_2$ NP/LIN dispersion was prepared by mixing LIN powder (21 mg) into TiO$_2$ paste (1.0 g, 19 wt %). Then, TAA (80 μL) and EtOH (9.92 mL) were added. The combined TiO$_2$ NP/LIN/TAA/EtOH dispersion was mixed with the aid of sonication. LIN/TiO$_2$ films were prepared by pipetting the dispersion (80 μL) onto ITO glass followed by spin coating at 2000 rpm for 30 s. The film was sintered as described above.

**Microgel/TiO$_2$ Film Preparation.** SPT/TiO$_2$ films prepared using S-MG or L-MG followed the same procedure. TiO$_2$ NP/MG dispersion was prepared by mixing MG dispersion (0.20 g/mL, 0.050 mL) into TiO$_2$ paste (1.0 g, 19 wt %). Then, TAA (80 μL) and EtOH (9.87 mL) were added. The combined TiO$_2$ NP/MG/TAA/EtOH dispersion was mixed with the aid of sonication. The spin-coating procedure and sintering conditions used to prepare the MG/TiO$_2$ films were the same as those described above for the LIN/TiO$_2$ film.

**Perovskite Film Preparation.** A PbI$_2$ solution (75 μL) containing PbI$_2$ (500 mg) at a concentration of 1.0 mM in a mixed solvent of DMF (950 μL) and DMSO (50 μL) was dropped onto the TiO$_2$ NP films on ITO and then spun at 1500 rpm for 30 s. The substrate was then placed onto a 70 °C hot plate and heated for 1.0 min and cooled to room temperature. Next, 100 μL of the double cation solution FAI (60 mg, 0.349 mM), MABr (6.0 mg, 0.054 mM), and MACl (6.0 mg, 0.089 mM) was added to 1.0 mL of the IPA solution and dropped onto the PbI$_2$ films. The substrate was then spun at 2000 rpm for 30 s. The FA$_{1-x}$MA$_x$Pb(I, Br, Cl)$_3$ film was transferred onto a 150 °C hot plate and annealed for 15 min. For XRD studies, PMMA/CBZ solution (10 mg/mL) was spin-coated onto the perovskite film at 4000 rpm for 10 s for encapsulation. The thicknesses of the SPT/TiO$_2$/PVK films prepared using L-MG, S-MG, LIN as SPTs and the control TiO$_2$ were measured (Dektak) to be 355 ± 14, 390 ± 19, 355 ± 9, and 346 ± 16 nm, respectively.

**Device Fabrication.** ITO glass (Ossila) was patterned using Zn powder and HCl (4.0 M), then cleaned with water and sonicated using acetone, IPA, and EtOH and washed with water, then dried under a N$_2$ stream, and then treated by UV-ozone plasma for 20 min. The TiO$_2$ blocking layer was deposited onto the cleaned ITO substrate by spin coating TIP solution (70 μL), 5000 rpm for 30 s and then sintered at 450 °C for 45 min. The SPT/TiO$_2$ or meso-TiO$_2$ films were then deposited using the conditions described above. After TiO$_2$ layer deposition, the substrates were transferred to a 2% humidity nitrogen-filled glovebox for the next stages of fabrication. The perovskite layer was prepared via a two-step method, as described above. A Spiro solution in CBZ (90 mg/mL) was mixed with TBP (34 μL), Li-TFSI solution (17 μL of 517 mg/mL in acetonitrile), and FK209 Co(III) TFSI (10 μL of 300 mg/mL in acetonitrile). The Spiro layer was spin-coated at 4000 rpm for 15 s. Finally, a Au counter electrode (80 nm) was deposited by thermal evaporation under high vacuum. A 0.080 cm$^2$ metal mask was used to define the active solar cell area.

**Physical Measurements.** Dynamic light scattering (DLS) measurements were conducted using a Malvern Zetasizer Nano ZS instrument and provided the z-average diameter ($d_z$). Scanning electron microscopy (SEM) was performed using an FEI Magellan 400 XHR FEG-SEM instrument. The TiO$_2$ films were measured using an accelerating voltage of 5 kV. The particle and pore sizes were measured by SEM. At least 100 particles or pores were counted. Perovskite films were measured under a 3 kV accelerating voltage. The cross section of solar cells was prepared via the focused ion beam (FIB) technique using an FEI Quanta 3D FIB/SEM system with multiple current and voltage approaches to minimize spatial sample damage. High-angle annular dark-field scanning transmission electron microscopy (HAADF-STEM) images were captured by using FEI Talos F200A ultrahigh brightness SuperX FEG (200 kV). Chemical analysis was performed using SuperX silicon drift detectors in the Talos, and the built-in pole piece of the objective lens enabled high-resolution and high-precision elemental mapping. The thickness of the films was measured using a Dektak XT profilometer. UV−visible spectra were obtained using a Hitachi U-1800 spectrophotometer. PL spectra were measured using a double monochromator FLS980 instrument (Edinburgh Instruments, U.K.). XRD patterns were obtained using a Bruker D8 Advance diffractometer (Cu Kα). TiO$_2$

and MGs atomic force microscopy (AFM) images were captured using a Bruker catalyst. Films were scanned using tapping mode. The Si AFM probe was purchased from Nunano. The probe was autotuned by the Nanoscope software; the drive frequency was 388 kHz. The scan rate was 0.25 Hz. Images were processed using the Nanoscope software. Perovskite film images were captured using JPK NanoWizard IV. The scanning rate was 6.5 Hz. Images were processed using the JPKSPM Data Processing software. EQE data were obtained using a Newport QuantX-300 instrument. A Micromeritics ASAP 2020 sorption analyzer was used to obtain $N_2$ adsorption/desorption isotherms at 77 K and to measure the Brunauer−Emmett−Teller (BET) surface area. Nitrogen adsorption/desorption isotherms were measured at 77 K using bulk samples heated at 500 °C for 2 h. Helium was used for the free space determination. The pore size distribution was determined using the BJH method. Electrochemical impedance spectroscopy (EIS) measurements were performed using phase-sensitive detection of the current using a lock-in amplifier. An AC voltage of 10 mV was applied, and the frequency swept between 1.0 Hz and 1 MHz. The voltage was supplied using an Agilent 33210A function generator. Ultraviolet photoemission spectroscopy (UPS) was performed using a HIS 13 high intensity VUV source (200 mA emission, Focus GmbH) within an ESCA2SR spectrometer (Scienta Omicron GmbH) using He II (40.5 eV) photons. Thermogravimetric analysis (TGA) was performed in air using a TA Instruments Q800 instrument. The LIN sample was heated in air from room temperature to 490 °C at 5 °C/min and then from 490 to 510 °C at 0.3 °C/min.

**Device Measurements.** Current−voltage measurements of the PSCs were measured under a class AAA solar simulator (Newport Oriel Sol3A) at AM1.5 and 100 mW/cm² illumination conditions and calibrated against a KG5 filtered silicon reference cell (Newport Oriel 91150-KG5) using a Smart PV and OLED Multiplexor Test Board. The J−V measurements were conducted in ambient air. The devices were measured following 30 s light soaking, with a 0.020 V/s scan rate and 0.1 s settling time unless otherwise stated. Both forward (short circuit to open circuit) and reverse (open circuit to short circuit) sweeps were measured.

## RESULTS AND DISCUSSION

**Soft Particle-Templated $TiO_2$ Nanoparticle Film Morphology.** We studied three SPT species in this work. Two SPTs were MGs (L-MG and S-MG) and the third was a commercially available linear polymer (LIN). All of the SPTs are composed of PNIPAm (Figure 1). PNIPAm was selected as the template polymer because it is soluble in EtOH, which is a key solvent used in $TiO_2$ pastes.[8,22,40] PNIPAm is a temperature-responsive polymer in water[41] and collapses (i.e., MG particles and LIN coils deswell) above 32 °C. At such temperatures, water is a bad solvent. DLS data for L-MG, S-MG, and LIN in EtOH (a good solvent) and water at 60 °C (a bad solvent) were obtained (see Figure S2A,B) and are discussed in the Supporting Information. MG particle volume swelling ratios ($\alpha_p$) in EtOH for L-MG and S-MG of 25 and 15, respectively, were calculated from the DLS data. These values show that the L-MG particles swelled more in EtOH than the S-MG particles. SEM images for the SPTs deposited from water at 60 °C are shown in Figure 2. The average diameters for L-MG, S-MG, and LIN obtained from SEM ($D_{SEM}$) are 264, 88, and 53 nm, respectively. The LIN particles are aggregates of collapsed polymer chains, whereas the MGs are individual particles. A summary of all of the SPT size data is presented in Table S1. All of the characterization data show that the SPT size decreases in the order L-MG > S-MG > LIN.

SPT/$TiO_2$ scaffolds were prepared following the method depicted in Figure 1. SEM images, pore size distributions, and average pore sizes for the nonannealed SPT/$TiO_2$ and meso-
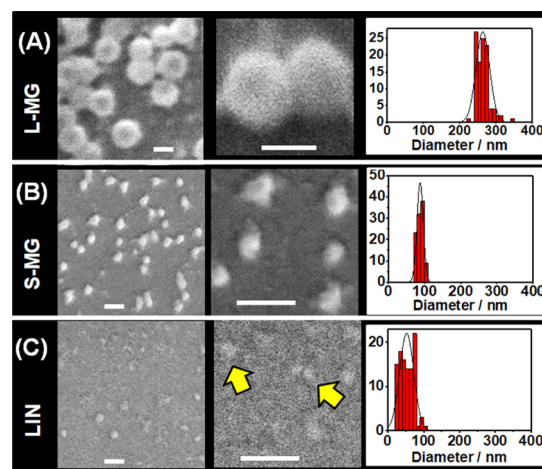


**Figure 2.** SEM and size distributions of (A) L-MG, (B) S-MG, and (C) LIN deposited under bad solvency conditions (water at 60 °C). The arrows in (C) indicate smaller LIN aggregates. The scale bars are 200 nm. The y-axes of the distributions show the number of particles counted.

$TiO_2$ films are shown in Figure S3. It is important to note that the SPTs were removed from all of the scaffolds in this study by sintering at 500 °C. This was demonstrated in three ways. First, L-MG microgel dispersion was placed on ITO-coated glass, which was heated at 500 °C on a hot plate. The solvent rapidly evaporated and then the polymer turned black and was completely burnt off within 397 s (See Movie S1 and Figure S4). Second, SEM images of L-MG before and after being heated at 500 °C were measured (See Figure S5). They show that the L-MG particles completely disappeared as a result of the heat treatment. Third, TGA data for LIN (Figure S6) show that ∼95% of the mass was lost as a consequence of heating to 500 °C. The discussions that follow concern SPT/$TiO_2$ and meso-$TiO_2$ layers annealed at 500 °C for 30 min unless otherwise stated.

SEM images for the MG- and LIN-templated $TiO_2$ films as well as the control meso-$TiO_2$ film are shown in Figure 3. Representative pores are highlighted by yellow arrows. While the MGs increased the pore size within the $TiO_2$ films when a concentration of 5 wt % was used (Figure 3A,B), we found that a LIN concentration of 10 wt % was required to achieve comparably large pores (Figure 3C). The pore size distributions measured from the SEM data (Figure 3) show that relatively large pores are present for the $TiO_2$ scaffold prepared using L-MG (Figure 3A), although a wide range of sizes is evident. The pore size distribution is relatively narrow for S-MG/$TiO_2$ (Figure 3B) and LIN/$TiO_2$ (Figure 3C). The average pore sizes measured for L-MG/$TiO_2$, S-MG/$TiO_2$, and LIN/$TiO_2$ films as well as the meso-$TiO_2$ film are 112 ± 86, 113 ± 49, 66 ± 33, and 37 ± 12 nm, respectively. This trend is similar to those for the films before annealing (see Figure S3) although the pore sizes had increased by a factor of about two due to annealing. The average pore sizes occupy a gap in the literature for pore size-adjusted $TiO_2$ films deposited in one step for PSCs. P123 polymer-adjusted meso-$TiO_2$ had a pore size of 16−34 nm,[14] whereas $TiO_2$ scaffolds prepared with a pore diameter of ∼200 nm were prepared using sacrificial PS particles.[13] The data in Figure 3 show that larger pores are produced with larger SPTs.

The final stages of the spin coating of the SPTs from EtOH will necessarily correspond to the collapsed PNIPAm state as
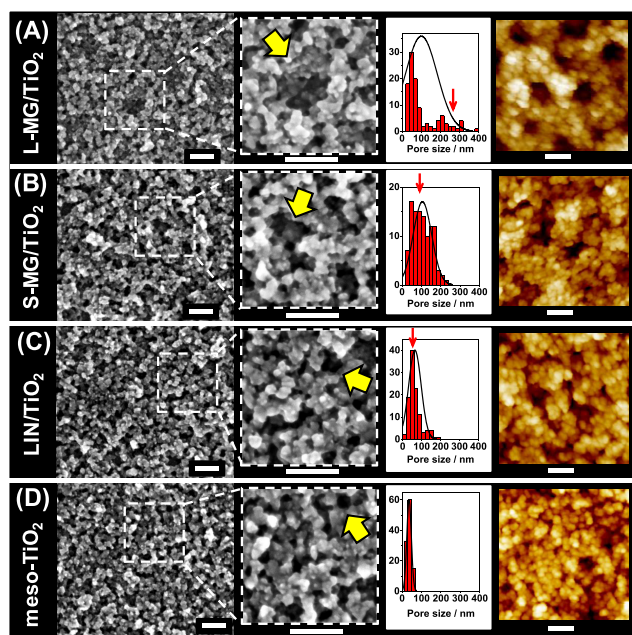
**Figure 3.** SEM, pore size distributions, and tapping mode AFM images for SPT/TiO$_2$ films of (A) L-MG/TiO$_2$, (B) S-MG/TiO$_2$, and (C) LIN/TiO$_2$. The control meso-TiO$_2$ film is shown in (D). The yellow arrows highlight pores. The red arrows in the distributions show the positions of the $D_{SEM}$ values for the respective SPT obtained from Figure 2. Scale bars: 200 nm.

EtOH evaporates. We therefore use the $D_{SEM}$ values for comparison with the pore sizes of the SPT/TiO$_2$ films. The $D_{SEM}$ values for L-MG, S-MG, and LIN are indicated by red arrows in the size distributions shown in Figure 3. For the S-MG/TiO$_2$ (Figure 3B) and LIN/TiO$_2$ (Figure 3C) films, the majority of the pores reside to the right of the respective $D_{SEM}$ values. This is what one would expect if the pores formed by TiO$_2$ NPs compressing partially swollen or collapsed SPTs. The relationship between collapsed L-MG size and the pore size distribution (Figure 3A) is less clear. While there are some pores similar or larger than $D_{SEM}$ (residing at and to the right of the red arrow), there is also a high proportion of pores residing to the left on the small size side. The latter may be due to L-MGs that deformed nonuniformly due to the relatively large shear stresses imposed during scaffold deposition via spin coating. L-MG swelled more strongly than S-MG (discussed above) and is also larger, which are two factors favoring deformation. L-MG is also lightly crosslinked. Lightly cross-linked, large, PNIPAm MGs are well known to be able to deform nonuniformly.[42]

The tapping mode AFM images in Figure 3 were obtained and confirmed the evolution of the pore diameter with the SPT size discussed above. Wider-area AFM image views and line profiles for the four TiO$_2$ films are shown in Figure S7. The RMS roughness values for the films decrease in the order: L-MG/TiO$_2$ (23.7 nm) > S-MG/TiO$_2$ (21.3 nm) > LIN/TiO$_2$ (18.7 nm)> control/TiO$_2$ (13.6 nm). These data demonstrate the ability of the larger SPTs to create a more undulating surface. The film thicknesses for L-MG/TiO$_2$, S-MG/TiO$_2$, LIN/TiO$_2$, and meso-TiO$_2$ film were 147 ± 26, 147 ± 14, 231 ± 12, and 135 ± 11 nm, respectively. The LIN/TiO$_2$ film was significantly thicker than the rest of the films. This may be due to the higher polymer content used for that film.

Nitrogen adsorption/desorption isotherms were measured for these systems. The minimum sample mass requirements necessitated the use of bulk scaffolds prepared by drop casting rather than spin coating. The pore size distributions appear in Figure S8. The average surface area values and pore sizes were 79−82 m$^2$/g and 21−22 nm, respectively. There was no measurable difference between these values for the different scaffolds. These results do not agree with both the TEM (Figure 3) and AFM (Figures 3 and S7) for the spin-coated scaffolds. This discrepancy is due to (a) the use of bulk samples, which meant that the scaffold formation mechanism lacked the rotational forces and large material loss of spin coating[43] and (b) the relative insensitivity of the BET method to pore sizes larger than ~20 nm.[44] It is suggested that SPT/TiO$_2$ morphology observed (Figure 3) is favored by spin coating. We use the TEM pore sizes for the discussions below.

The ability of light to pass through the SPT/TiO$_2$ films is important for solar cell applications. Transmittance spectra of the films were measured (Figure S9A) and are similar to those reported elsewhere for TiO$_2$ films.[45] The spectra show that the LIN/TiO$_2$ film had the lowest average transmittance (71.3%) over the 300−800 nm range (Figure S9B). This is because the LIN/TiO$_2$ film was thicker than other SPT/TiO$_2$ films and meso-TiO$_2$, as discussed above. The S-MG/TiO$_2$ and L-MG/TiO$_2$ films had average transmittance values of 76.1 and 77.2%, respectively. These values are only slightly less than that measured for the meso-TiO$_2$ film of 78.6%.

**Perovskite Films Prepared Using SPT/TiO$_2$ Films.** We next prepared perovskite films using the two-step method depicted in Figure 1. SEM images and grain size distributions obtained from the SEM data are shown in Figure 4. Large grains (with many greater than 1 $\mu$m) can be seen in the films prepared using each of the SPT/TiO$_2$ films (Figure 4A−C). In contrast, smaller grains are present for the meso-TiO$_2$/PVK film (Figure 4D). (Larger area SEM images are shown in Figure S10.) The average grain sizes for the films grown using L-MG/TiO$_2$, S-MG/TiO$_2$, LIN/TiO$_2$, and meso-TiO$_2$ films are 865 ± 175, 755 ± 215, 660 ± 225, and 570 ± 170 nm, respectively. Hence, the average grain sizes decreased in the order: L-MG/TiO$_2$/PVK > S-MG/TiO$_2$/PVK > LIN/TiO$_2$/PVK > meso-TiO$_2$/PVK. Importantly, this order follows that of the $D_{SEM}$ values (Table S1). However, this order does not fully agree with the average pore sizes discussed above because the average pore sizes were not distinguishable for L-MG and S-MG. This result implies that crystals grown from the largest pores within the distribution of pores dominated the final crystal size.

AFM images were obtained for the films and are also shown in Figure 4. (Larger area AFM images and line profiles are shown in Figure S11.) The differences in the crystal size discussed above are confirmed by the AFM data. The RMS roughness values for the films grown using L-MG/TiO$_2$, S-MG/TiO$_2$, LIN/TiO$_2$, and meso-TiO$_2$ films are 22.1, 25.3, 22.2, and 19.9 nm, respectively, based on line profiles. Hence, the SPT/TiO$_2$/PVK films have greater roughness than the control meso-TiO$_2$/PVK film. The RMS roughness values for the underlying SPT/TiO$_2$ scaffolds were also greater than that for the meso-TiO$_2$ scaffold (see above). Differences in the initial heights of the TiO$_2$ scaffold can be expected to be approximately translated to the final PVK films if capping layers recrystallize on the scaffolds.[46] In addition, the increased grain size of the SPT/TiO$_2$/PVK films likely also contributes to their increased roughness.
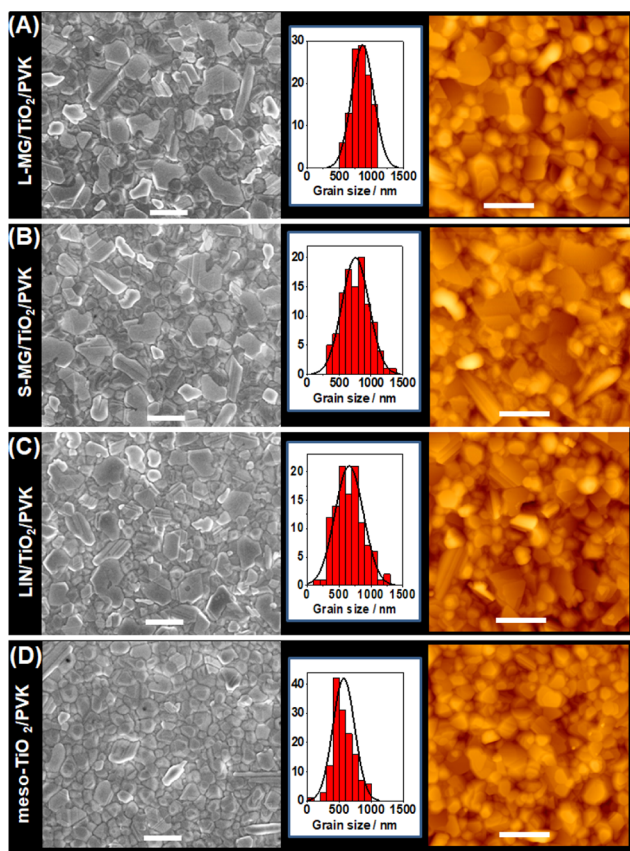
**Figure 4.** SEM, grain size distributions, and tapping mode AFM images for (A) L-MG/TiO$_2$/PVK, (B) S-MG/TiO$_2$/PVK, (C) LIN/TiO$_2$/PVK, and (D) meso-TiO$_2$/PVK films. Scale bars: 1 $\mu$m.

The increased grain size for the SPT/TiO$_2$/PVK films likely originates from less restriction during crystal growth as perovskite crystal domain size can be constrained by the pore size of preformed TiO$_2$ scaffolds.[27] Furthermore, an increase in the pore size for the meso-TiO$_2$ layer is known to increase PbI$_2$ infiltration[47] due to faster and less obstructed mass transport. Fu et al. proposed a dissolution/recrystallization model for two-step deposition[46] wherein supply of PbI$_2$ from within the scaffold to the surface caused MAPI crystals to grow in the capping layer. For the present TiO$_2$ scaffolds, as the pore size of the SPT TiO$_2$ scaffold increases, the rate of supply of PbI$_2$ should also increase, which is proposed to increase the rate of crystal growth and hence the PVK grain size. To test this proposal, we prepared a planar PVK film without any scaffold and hence without obstruction for crystal growth. The SEM images also showed many large grains (see Figure S12). The average grain size was 867 ± 438 nm. While the average grain size is indistinguishable from that for the L-MG/TiO$_2$/PVK film (Figure 4A), the grain size distribution for the planar PVK film is far more polydisperse. This result suggests a beneficial effect of our SPT/TiO$_2$ approach in delivering films with more uniform grain sizes compared to planar PVK films.

Devices were prepared using the SPT/TiO$_2$ films and the architecture is depicted in Figure 5A. Data from the champion S-MG/TiO$_2$ PSC cell are shown in Figure 5B, which had a PCE of 18.8%. The device performance data extracted from the $J$–$V$ curves are shown in Figure 5C–F and these values are tabulated in Table S2. The highest average $V_{oc}$ was 1.04 V for the S-MG/TiO$_2$/PVK system (Figure 5C). Furthermore, the $V_{oc}$ values for the SPT/TiO$_2$-based PSCs were all significantly larger than those for the meso-TiO$_2$-based PSC. This is
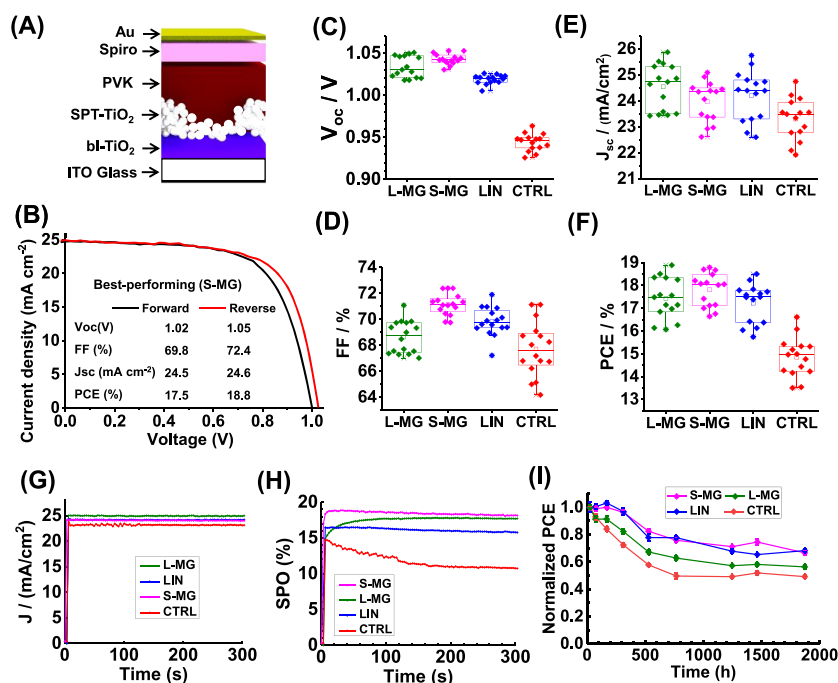


**Figure 5.** (A) Device architecture. (B) $J$–$V$ characteristics for the best-performing device, which was prepared using S-MG/TiO$_2$. Statistics for solar cell performance with the various SPT/TiO$_2$ scaffolds and the control meso-TiO$_2$ are shown in (C)–(F). The performance parameters are (C) open-circuit voltage, (D) fill factor, (E) short-circuit current density, and (F) PCE. (G) Current density and (H) steady-state power output (SPO). (I) Evolution of normalized power conversion efficiency with time. The devices (not encapsulated) were kept in ambient air between measurements and the humidity varied between 40 and 90%.

attributed to the increased grain sizes for the SPT/$TiO_2$ systems noted above since $V_{oc}$ for PSCs is known to increase with the grain size.[48] Grain boundaries are well known to contain defects and have a high density of trap states.[49] Traps favor nonradiative recombination, which decreases $V_{oc}$.[50,50] Hence, because our devices prepared with the SPT/$TiO_2$ films have larger grains, they have fewer traps and higher $V_{oc}$ values compared to the system prepared using meso-$TiO_2$, which had smaller grains.

The fill factor (FF) and $J_{sc}$ values are also higher for the devices prepared using SPT/$TiO_2$ films than for the meso-$TiO_2$ films (Figure 5D,E). This result is expected because increases in $V_{oc}$ are theoretically linked to increases in $J_{sc}$ (and EQE).[51] The devices prepared using S-MG/$TiO_2$ had the greatest reproducibility and highest average PCE of 17.8% (Figure 5F). The average PCE values are clearly higher for the films prepared using SPT/$TiO_2$ compared to that prepared using meso-$TiO_2$ (14.9%). The average PCE values for the S-MG/$TiO_2$/PVK and L-MG/$TiO_2$/PVK (17.4%) devices were close to that for the LIN/$TiO_2$/PVK devices (17.2%). Hence, it can be concluded that using SPT/$TiO_2$ films (either MGs or LIN) gave a similar large increase in PCE (an increase of ~20%) compared to the control meso-$TiO_2$ system. The variation of $J$ with time (Figure 5G) and steady-state power output (SPO, Figure 5H) were measured. The SPO values for the SPT/$TiO_2$/PVK devices showed much better stability compared to the control. All of these data augur well for versatility and potential widespread use of our new method as the MGs are easily prepared using a scalable preparation. Crucially, LIN is commercially available.

Hysteresis is an important topic for PSCs[52,53] because it is a source of instability that affects PSC performance. The hysteresis index (HI) for devices prepared using L-MG/$TiO_2$, S-MG/$TiO_2$, LIN/$TiO_2$, and meso-$TiO_2$ was calculated using the normalized difference between the reverse and forward PCE values.[54] We investigated the effect of the scan rate on the HI over the range of 0.020−0.20 V/s. The data (Table S3) show that the variations in the HI values with the scan rate were modest and a clear trend was not present for all samples. It follows that there are no large differences in the sweep-rate-induced ion accumulation between the samples over the sweep ranges studied. The average HI values for L-MG/$TiO_2$, S-MG/$TiO_2$, LIN/$TiO_2$, and meso-$TiO_2$ are 5.8, 6.0, 4.4, and 2.4%, respectively (see Figure S13). Hence, the HI increased using SPT/$TiO_2$. However, the HI was relatively low for all cases (≤6%). Our trend is opposite to that reported by Shao et al.[14] Planar PSCs are generally known to have greater HI values than meso-$TiO_2$-based PSCs.[52] This is because of less perovskite/electron-transport layer contact for planar devices, which results in slower electron extraction. Fast extraction of electrons is aided by meso-$TiO_2$ due to the high surface area and this is known to give low HI values.[55] Because the SPT/$TiO_2$ films had larger pores than meso-$TiO_2$ (Figure 3), the perovskite/$TiO_2$ contact area decreased, which would account for the relative increase of HI observed.[56] In regard to achieving a balance between PCE and HI, the LIN/$TiO_2$-based device has an optimum balance of improved PCE (average of 17.2%) and low HI (average of 4.4%).

The variation of the normalized PCE for nonencapsulated devices exposed to ambient conditions is shown in Figure 5I. The variation of $V_{oc}$, $J_{sc}$ and FF appears in Figure S14A−C. The stability of all of the devices decreased at first and then plateaued. The LIN/$TiO_2$ devices maintained ~70% of their

initial PCE after 1870 h (78 days) and had the best stability (Figure 5I). The values for S-MG/$TiO_2$ (67%) and L-MG/$TiO_2$ (56%) were higher than those of the control meso-$TiO_2$ system (49%). Moisture-induced degradation begins at grain boundaries and proceeds inward.[57] Larger grain sizes provide smaller surface area-to-volume ratios, which slow the rate of moisture degradation.[58] We attribute the better stability of the SPT/$TiO_2$ devices to the larger grain sizes compared to the control prepared using meso-$TiO_2$ (as shown in Figure 4).

**Investigating Origin of Performance Increase for SPT/$TiO_2$/PVK Devices.** An intriguing question is why the devices prepared using the SPT/$TiO_2$ had higher PCEs than those prepared using meso-$TiO_2$. We investigated the structures of the perovskite films using X-ray scattering (Figure S15). The scattering profiles are ascribed to the cubic $\alpha$-perovskite phase and are similar to those reported for related perovskites.[59,60] There are no clear differences for the perovskite phase. Residual $PbI_2$ is present for the films prepared using S-MG/$TiO_2$ and LIN/$TiO_2$ but mostly absent for the films prepared using L-MG/$TiO_2$ and meso-$TiO_2$. We examined a cross section of an ITO/bl-$TiO_2$/S-MG/$TiO_2$/PVK/Spiro/Au device using HAADF-STEM (see Figure 6A).
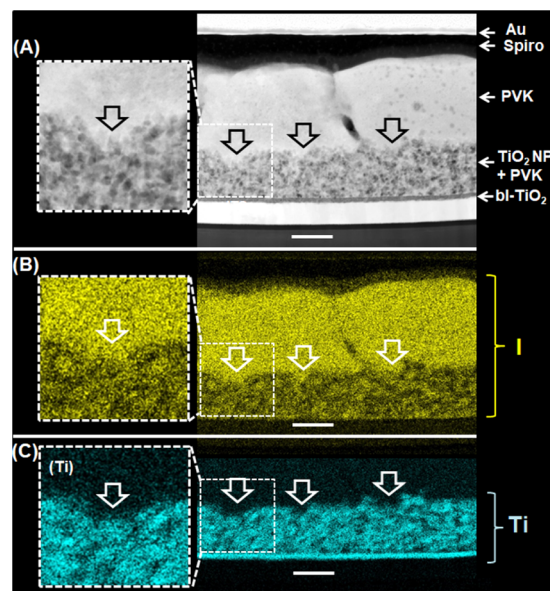


**Figure 6.** (A) HAADF-STEM image for an ITO/bl-$TiO_2$/S-MG/$TiO_2$/PVK/Spiro/Au device. Images measured using (B) I and (C) Ti elemental mapping are shown. The arrows highlight regions where S-MG particles had created surface pores prior to their removal. Scale bars: 200 nm.

The arrows highlight three regions where S-MGs had created surface pores. Such pores can also be seen in Figure 3B (arrow). The elemental mapping shows clearly the presence of I in the surface pores (arrow) as well as infiltration within the scaffold interior (Figure 6B). The Ti mapping (Figure 6C) shows the surface pores templated by S-MG clearly. Comparison of Figure 6B,C implies that the perovskite capping layer grew from the perovskite within the surface pores left by the S-MG templates. This suggestion is congruent with the report of Pascoe et al., who noted that crystals grow larger in unrestricted systems, such as planar films.[61]

UV−visible spectra of the films are shown in Figure 7A. The S-MG/$TiO_2$/PVK film had the highest absorbance. This is
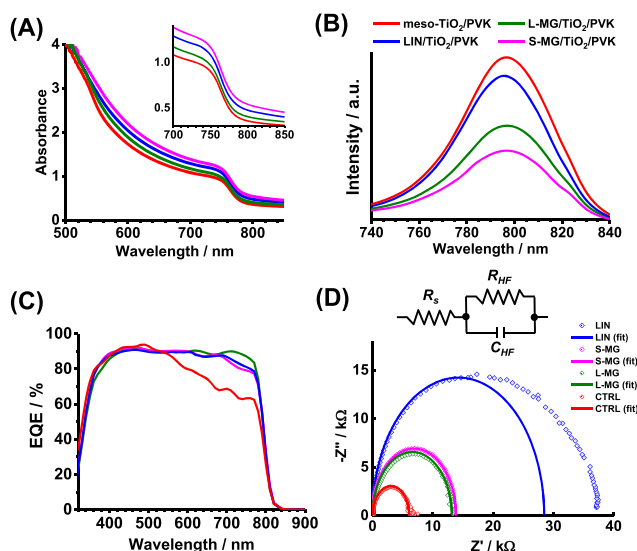
**Figure 7.** (A) UV−visible and (B) PL spectra for ITO/bl-TiO$_2$/SPT/TiO$_2$/PVK and ITO/bl-TiO$_2$/meso-TiO$_2$/PVK films. The excitation wavelength was 470 nm. (C) EQE spectra for devices. The legend in (B) applies to (A)−(C). (D) Nyquist plots and the equivalent circuit diagram for the devices. Z′ and Z″ are the real and imaginary components of the complex impedance, respectively. $R_s$, $R_{HF}$, and $C_{HF}$ are the series resistance, high-frequency resistance, and high-frequency capacitance. An extended model that gives an improved fit to the LIN-based data is shown in Figure S16.

because that film had the largest thickness and roughness (above). The absorbance values for L-MG/TiO$_2$/PVK and LIN/TiO$_2$/PVK films are also greater than those for the meso-TiO$_2$/PVK film. The absorption onsets were all ∼785 nm and unaffected by the pore size. PL spectra were also obtained (Figure 7B). Those data show quenching increases in the substrate order: meso-TiO$_2$ < LIN/TiO$_2$ < L-MG/TiO$_2$ < S-MG/TiO$_2$. This result implies more efficient electron transport to the TiO$_2$ scaffold from L-MG/TiO$_2$/PVK and S-MG/TiO$_2$/PVK films compared to LIN/TiO$_2$/PVK and meso-TiO$_2$/PVK. This would be expected from the larger grain sizes for the films (above) since grain boundaries act as an impediment to charge transport.[62]

We measured the EQE for the devices (Figure 7C). The integrated current densities for the devices prepared using L-MG/TiO$_2$, S-MG/TiO$_2$, LIN/TiO$_2$, and meso-TiO$_2$ devices were 23.4, 23.1, 23.1, and 21.2 mA/cm$^2$, respectively. All of these values are lower than those measured from the J−V curves (Table S2) by an average of 6%. Interestingly, the EQE spectra for the SPT/TiO$_2$/PVK films are very similar and there is a pronounced increase in the EQE for these systems at wavelengths greater than 500 nm compared to that for meso-TiO$_2$/PVK. Ye et al.[63] attributed enhancements in EQE at such wavelengths to an optical interference effect caused by TiO$_2$ NP scattering. The pores for the SPT/TiO$_2$ films are substantially larger than those for the control film (Figure 3) and relatively intense light scattering is expected. Furthermore, enhanced light scattering from the increased roughness of the SPT/TiO$_2$/PVK film surfaces (discussed above) is also expected to have increased the EQE through increased light absorption. Indeed, higher absorption for the SPT/TiO$_2$/PVK films was noted above for Figure 7A. Theoretical studies have also predicted increased EQE values for PVK films that scatter more light.[64] While increased light scattering appears to have

contributed to the increased PCE of the SPT/TiO$_2$-based PSCs compared to the control meso-TiO$_2$ system, the grain size differences apparent from SEM (and AFM) are likely the main reason for the PCE improvement.[65]

EIS measurements were performed for the devices, and the real (Z′) and imaginary (−Z″) components of the impedance are shown in Figure 7D. The data were measured in the dark with a bias of $V_{oc}$. A single recombination semicircle indicates that only one type of charge transport dominated[66] and has also been reported elsewhere.[67] We initially used a simple ideal semiconductor equivalent circuit model[68] to fit the data (Figure 7D). The parameters $R_s$, $R_{HF}$, and $C_{HF}$ are the series resistance, high-frequency resistance, and high-frequency capacitance, respectively. The values from the fits are shown in Table S4. Because the frequencies for the maxima were greater than 300 MHz, the data are associated with the recombination of free carriers.[69] $R_{HF}$ increases with the semicircle size and is inversely proportional to the recombination rate.[70] The latter was lowest for the meso-TiO$_2$/PVK device, which had the lowest $J_{sc}$ (Table S2). The electron lifetime ($\tau_{HF} = R_{HF}C_{HF}$) was calculated[66] (Table S4). The value for meso-TiO$_2$ of 95 $\mu$s is close to that reported elsewhere.[67] The $\tau_{HF}$ values for the SPT/TiO$_2$/PVK devices (135−325 $\mu$s) are all much higher than those for meso-TiO$_2$/PVK. This is due to the larger grain sizes of the SPT/TiO$_2$/PVK films (Figure 3) because the increased grain size results in less recombination at grain boundaries[56] and higher diffusion lengths.[71] The fit for LIN/TiO$_2$/PVK is improved by adding an additional RC circuit element[72] (Figure S16), and the fitted data are shown in the last row of Table S4. The value for $\tau_{HF}$ decreases to 265 $\mu$s but remains much greater than that for the meso-TiO$_2$/PVK control. The EIS data support the view that the increased grain size is responsible for the higher PCEs of the SPT/TiO$_2$/PVK systems.

Figure S17 shows the UPS valence spectra for the SPT/TiO$_2$/PVK and meso-TiO$_2$/PVK films. The energy difference between the valence band and the Fermi level ($E_F$) was 0.67 to 0.70 eV for all of the films and was not distinguishable. The spectral features and values are similar to those reported elsewhere for related systems.[73,74] The UV−visible spectra (Figure 7A) show that the absorption onsets were similar (∼760 nm), which implies that significant bandgap differences between the systems were not present. Hence, the increased porosity for the SPT/TiO$_2$/PVK did not significantly affect $E_F$ or the positions of the valence or conduction band edges for PVK in these systems.

The performance improvement of the SPT/TiO$_2$/PVK devices occurs despite the decreased interfacial contact between PVK and the TiO$_2$ scaffold that resulted from the increased pore size. Hwang et al. noted that improvement in the grain size of their devices dominated a decreased PVK/TiO$_2$ interfacial area and attributed this to a decrease in the number of PVK/interface trap sites.[13] The results of this study support the conjecture that an improvement in the PVK grain size can be more important for increasing PCE than a decrease of the PVK/TiO$_2$ area. Following a comment from a reviewer, we conducted a two-probe resistance test for ITO annealed at 500 °C for 30 min. The resistance increased from 75 to 245 Ω due to the annealing treatment. This trend is in agreement with the literature for ITO.[75] Because FTO is stable to such annealing,[76] it follows that the PCEs reported here could be further increased by replacing ITO with FTO. This will be pursued in future work.

## CONCLUSIONS

In summary, we have investigated the use of three pore size engineering additives to prepare SPT/TiO$_2$ scaffolds. They were MGs of two different sizes as well as linear PNIPAM. The MGs were prepared using a scaleable method and the LIN is commercially available. All three SPTs gave meso-TiO$_2$ with an increased pore size, which in turn increased the perovskite grain size. The PSCs for all three systems prepared from SPT/TiO$_2$ had substantially higher PCE values and stabilities than those of the control prepared with the meso-TiO$_2$. This improvement was due to a combination of increased perovskite grain size as well as improved charge transfer and light scattering. The study has shown that SPTs can increase the perovskite grain size via the pore size increase of the TiO$_2$ NP layer. The one-step SPT engineering approach to prepare pore-controlled TiO$_2$ films using scalable and commercially available polymer additives introduced in this study should apply to other PSCs.

## ASSOCIATED CONTENT

### ⓈⒾ Supporting Information

The Supporting Information is available free of charge at https://pubs.acs.org/doi/10.1021/acsami.0c02248.

Comparison of the present work with previous PSC studies involving MGs, DLS data for MGs and LIN with discussion, video and photographs and SEM of L-MG being burnt off an ITO surface, TGA of LIN being heated to 500 °C, TiO$_2$ AFM images and line profiles, hysteresis index data, sintered TiO$_2$ transmittance spectra and average transmittance values, pore size distribution data, large-area SEM images for non-annealed and annealed SPT/TiO$_2$ as well as SPT/TiO$_2$/PVK films and a planar PVK film, device stability data, X-ray scattering patterns, electrochemical impedance spectroscopy data, UPS spectra, SPT particle size data, $J$−$V$ figures of merit data (PDF)

A few drops of L-MG microgel dispersion was placed on ITO-coated glass, which was heated to 500 °C on a hot plate; water quickly evaporated and L-MG turned black and then is completely burnt off after only 397 s; photographs from the video are shown in Figure S4 (Movie S1) (MOV)

## AUTHOR INFORMATION

### Corresponding Authors

**Qing Lian** − *Department of Materials, University of Manchester, Manchester M1 3BB, United Kingdom*; Email: qing.lian@machester.ac.uk

**Brian R. Saunders** − *Department of Materials, University of Manchester, Manchester M1 3BB, United Kingdom*; ⓘ orcid.org/0000-0003-1410-2967; Email: brian.saunders@manchester.ac.uk

### Authors

**Muhamad Z. Mokhtar** − *Department of Materials, University of Manchester, Manchester M1 3BB, United Kingdom*

**Dongdong Lu** − *Department of Materials, University of Manchester, Manchester M1 3BB, United Kingdom*

**Mingning Zhu** − *Department of Materials, University of Manchester, Manchester M1 3BB, United Kingdom*

**Janet Jacobs** − *Photon Science Institute, The University of Manchester, Manchester M13 9PL, United Kingdom*

**Andrew B. Foster** − *Department of Chemistry, University of Manchester, Manchester M13 9PL, United Kingdom*; ⓘ orcid.org/0000-0001-8222-673X

**Andrew G. Thomas** − *Department of Materials, University of Manchester, Manchester M1 3BB, United Kingdom; Photon Science Institute and The Henry Royce Institute, The University of Manchester, Manchester M13 9PL, United Kingdom*; ⓘ orcid.org/0000-0002-1900-6686

**Ben F. Spencer** − *Department of Materials, University of Manchester, Manchester M1 3BB, United Kingdom; The Henry Royce Institute, The University of Manchester, Manchester M13 9PL, United Kingdom*; ⓘ orcid.org/0000-0002-1453-5327

**Shanglin Wu** − *Department of Materials, University of Manchester, Manchester M1 3BB, United Kingdom*

**Chen Liu** − *Department of Materials, University of Manchester, Manchester M1 3BB, United Kingdom*

**Nigel W. Hodson** − *BioAFM Facility, Faculty of Biology, Medicine and Health, Stopford Building, University of Manchester, Manchester M13 9PT, United Kingdom*

**Benjamin Smith** − *SPECIFIC, College of Engineering, Swansea University Bay Campus, Swansea SA1 8EN, United Kingdom*

**Abdulaziz Alkaltham** − *Department of Materials, University of Manchester, Manchester M1 3BB, United Kingdom*

**Osama M. Alkhudhari** − *Department of Materials, University of Manchester, Manchester M1 3BB, United Kingdom*

**Trystan Watson** − *SPECIFIC, College of Engineering, Swansea University Bay Campus, Swansea SA1 8EN, United Kingdom*; ⓘ orcid.org/0000-0002-8015-1436

Complete contact information is available at:
https://pubs.acs.org/10.1021/acsami.0c02248

### Notes

The authors declare no competing financial interest.

## REFERENCES

(1) Kojima, A.; Teshima, K.; Shirai, Y.; Miyasaka, T. Organometal Halide Perovskites as Visible-light Sensitizers for Photovoltaic Cells. *J. Am. Chem. Soc.* **2009**, *131*, 6050−6051.

(2) NREL Best Research-cell Efficiencies, 2020. www.nrel.gov/pv/cell-efficiency.html.

(3) Heo, J. H.; Im, S. H.; Noh, J. H.; Mandal, T. N.; Lim, C.-S.; Chang, J. A.; Lee, Y. H.; Kim, H.-j.; Sarkar, A.; Nazeeruddin, M. K.; Grätzel, M.; Seok, S. I. Efficient Inorganic−organic Hybrid Heterojunction Solar Cells Containing Perovskite Compound and Polymeric Hole Conductors. *Nat. Photonics* **2013**, *7*, 486−491.

(4) Pham, H. D.; Jain, S. M.; Li, M.; Manzhos, S.; Feron, K.; Pitchaimuthu, S.; Liu, Z.; Motta, N.; Wang, H.; Durrant, J. R.; Sonar, P. Dopant-free Novel Hole-transporting Materials Based on Quinacridone Dye for High-performance and Humidity-stable Mesoporous Perovskite Solar Cells. *J. Mater. Chem. A* **2019**, *7*, 5315−5323.

(5) Bandara, R. M. I.; Jayawardena, K. D. G. I.; Adeyemo, S. O.; Hinder, S. J.; Smith, J. A.; Thirimanne, H. M.; Wong, N. C.; Amin, F.

M.; Freestone, B. G.; Parnell, A. J.; Lidzey, D. G.; Joyce, H. J.; Sporea, R. A.; Silva, S. R. P. Tin(iv) Dopant Removal Through Anti-solvent Engineering Enabling Tin Based Perovskite Solar Cells with High Charge Carrier Mobilities. *J. Mater. Chem. C* 2019, 7, 8389−8397.

(6) Bae, S.; Jo, J. W.; Lee, P.; Ko, M. J. Controlling the Morphology of Organic−Inorganic Hybrid Perovskites Through Dual Additive-Mediated Crystallization for Solar Cell Applications. *ACS Appl. Mater. Interfaces* 2019, 11, 17452−17458.

(7) Li, C.; Yin, J.; Chen, R.; Lv, X.; Feng, X.; Wu, Y.; Cao, J. Monoammonium Porphyrin for Blade-Coating Stable Large-Area Perovskite Solar Cells with >18% Efficiency. *J. Am. Chem. Soc.* 2019, 141, 6345−6351.

(8) Giordano, F.; Abate, A.; Correa Baena, J. P.; Saliba, M.; Matsui, T.; Im, S. H.; Zakeeruddin, S. M.; Nazeeruddin, M. K.; Hagfeldt, A.; Graetzel, M. Enhanced Electronic Properties in |Mesoporous TiO2 via Lithium Doping for High-efficiency Perovskite Solar Cells. *Nat. Commun.* 2016, 7, No. 10379.

(9) Cui, Q.; Zhao, X.; Lin, H.; Yang, L.; Chen, H.; Zhang, Y.; Li, X. Improved Efficient Perovskite Solar Cells Based on Ta-doped TiO2 Nanorod Arrays. *Nanoscale* 2017, 9, 18897−18907.

(10) Ranjan, R.; Prakash, A.; Singh, A.; Singh, A.; Garg, A.; Gupta, R. K. Effect of Tantalum Doping in a TiO2 Compact Layer on the Performance of Planar Spiro-OMeTAD Free Perovskite Solar Cells. *J. Mater. Chem. A* 2018, 6, 1037−1047.

(11) Yin, X.; Guo, Y.; Xue, Z.; Xu, P.; He, M.; Liu, B. Performance Enhancement of Perovskite-sensitized Mesoscopic Solar Cells using Nb-doped TiO2 Compact Layer. *Nano Res.* 2015, 8, 1997−2003.

(12) Cheng, C.; Lee, M. M.; Noel, N. K.; Hughes, G. M.; Ball, J. M.; Assender, H. E.; Snaith, H. J.; Watt, A. A. R. Polystyrene Templated Porous Titania Wells for Quantum Dot Heterojunction Solar Cells. *ACS Appl. Mater. Interfaces* 2014, 6, 14247−14252.

(13) Hwang, T.; Lee, S.; Kim, J.; Kim, J.; Kim, C.; Shin, B.; Park, B. Tailoring the Mesoscopic TiO2 Layer: Concomitant Parameters for Enabling High-Performance Perovskite Solar Cells. *Nanoscale Res. Lett.* 2017, 12, 57.

(14) Shao, J.; Yang, S.; Lei, L.; Cao, Q.; Yu, Y.; Liu, Y. Pore Size Dependent Hysteresis Elimination in Perovskite Solar Cells Based on Highly Porous TiO2 Films with Widely Tunable Pores of 15−34 nm. *Chem. Mater.* 2016, 28, 7134−7144.

(15) Yang, Y.; Ri, K.; Mei, A.; Liu, L.; Hu, M.; Liu, T.; Li, X.; Han, H. The Size Effect of TiO2 Nanoparticles on a Printable Mesoscopic Perovskite Solar Cell. *J. Mater. Chem. A* 2015, 3, 9103−9107.

(16) Seo, J.; Noh, J. H.; Seok, S. I. Rational Strategies for Efficient Perovskite Solar Cells. *Acc. Chem. Res.* 2016, 49, 562−572.

(17) Zhao, Y.; Xu, X.; Zhang, H.; Shi, J.; Zhu, L.; Wu, H.; Li, D.; Luo, Y.; Meng, Q. Sequential Multi-drop Coating Method for Large Crystallized α-(NH2)2CHPbI3 and Mixed-organic-cation Perovskite Films for Highly Efficient Mesoscopic Perovskite Solar Cells. *J. Power Sources* 2017, 359, 147−156.

(18) Wozny, S.; Yang, M.; Nardes, A. M.; Mercado, C. C.; Ferrere, S.; Reese, M. O.; Zhou, W.; Zhu, K. Controlled Humidity Study on the Formation of Higher Efficiency Formamidinium Lead Triiodide-Based Solar Cells. *Chem. Mater.* 2015, 27, 4814−4820.

(19) Guo, D.; Yu, J.; Fan, K.; Zou, H.; He, B. Nanosheet-based Printable Perovskite Solar Cells. *Sol. Energy Mater. Sol. Cells* 2017, 159, 518−525.

(20) Gamliel, S.; Popov, I.; Cohen, B.-E.; Uvarov, V.; Etgar, L. Structural and Quantitative Investigation of Perovskite Pore Filling in Mesoporous Metal Oxides. *Crystals* 2016, 6, 149.

(21) Wang, Q.; Jiang, C.; Zhang, P.; Hamann, T. W. Overcoming Bulk Recombination Limits of Layered Perovskite Solar Cells with Mesoporous Substrates. *J. Phys. Chem. C* 2018, 122, 14177−14185.

(22) Ravishankar, S.; Gharibzadeh, S.; Roldán-Carmona, C.; Grancini, G.; Lee, Y.; Ralaiarisoa, M.; Asiri, A. M.; Koch, N.; Bisquert, J.; Nazeeruddin, M. K. Influence of Charge Transport Layers on Open-Circuit Voltage and Hysteresis in Perovskite Solar Cells. *Joule* 2018, 2, 788−798.

(23) Jung, K.; Lee, J.-H.; Oh, K.; Im, C.; Do, J.; Kim, J.; Chae, W.-S.; Lee, M.-J. Efficient Composition Tuning via Cation Exchange and Improved Reproducibility of Photovoltaic Performance in FA MA1-PbI3 Planar Heterojunction Solar Cells Fabricated by a Two-step Dynamic Spin-coating Process. *Nano Energy* 2018, 54, 251−263.

(24) Xiao, Y.; Wang, C.; Kondamareddy, K. K.; Cheng, N.; Liu, P.; Qiu, Y.; Qi, F.; Kong, S.; Liu, W.; Zhao, X.-Z. Efficient Electron Transport Scaffold Made up of Submicron TiO2 Spheres for High-Performance Hole-Transport Material Free Perovskite Solar Cells. *ACS Appl. Energy Mater.* 2018, 1, 5453−5462.

(25) Ramos, F. J.; Oliva-Ramirez, M.; Nazeeruddin, M. K.; Grätzel, M.; González-Elipe, A. R.; Ahmad, S. Nanocolumnar 1-dimensional TiO2 Photoanodes Deposited by PVD-OAD for Perovskite Solar Cell Fabrication. *J. Mater. Chem. A* 2015, 3, 13291−13298.

(26) Hernández-Granados, A.; Corpus-Mendoza, A. N.; Moreno-Romero, P. M.; Rodríguez-Castañeda, C. A.; Pascoe-Sussoni, J. E.; Castelo-González, O. A.; Menchaca-Campos, E. C.; Escorcia-García, J.; Hu, H. Optically Uniform Thin Films of Mesoporous TiO2 for Perovskite Solar Cell Applications. *Opt. Mater.* 2019, 88, 695−703.

(27) Hörantner, M. T.; Zhang, W.; Saliba, M.; Wojciechowski, K.; Snaith, H. J. Templated Microstructural Growth of Perovskite Thin Films via Colloidal Monolayer Lithography. *Energy Environ. Sci.* 2015, 8, 2041−2047.

(28) Li, T.; Pan, Y.; Wang, Z.; Xia, Y.; Chen, Y.; Huang, W. Additive Engineering for Highly Efficient Organic−inorganic Halide Perovskite Solar Cells: Recent Advances and Perspectives. *J. Mater. Chem. A* 2017, 5, 12602−12652.

(29) Mahapatra, A.; Prochowicz, D.; Tavakoli, M. M.; Trivedi, S.; Kumar, P.; Yadav, P. A Review of Aspects of Additive Engineering in Perovskite Solar Cells. *J. Mater. Chem. A* 2020, 8, 27−54.

(30) Zuo, L.; Guo, H.; deQuilettes, D. W.; Jariwala, S.; De Marco, N.; Dong, S.; DeBlock, R.; Ginger, D. S.; Dunn, B.; Wang, M.; Yang, Y. Polymer-modified Halide Perovskite Films for Efficient and Stable Planar Heterojunction Solar Cells. *Sci. Adv.* 2017, 3, No. e1700106.

(31) Li, H.; Wu, G.; Li, W.; Zhang, Y.; Liu, Z.; Wang, D.; Liu, S. Additive Engineering to Grow Micron-Sized Grains for Stable High Efficiency Perovskite Solar Cells. *Adv. Sci.* 2019, 6, No. 1901241.

(32) Wu, Y.; Xie, F.; Chen, H.; Yang, X.; Su, H.; Cai, M.; Zhou, Z.; Noda, T.; Han, L. Thermally Stable MAPbI3 Perovskite Solar Cells with Efficiency of 19.19% and Area over 1 cm2 Achieved by Additive Engineering. *Adv. Mater.* 2017, 29, No. 1701073.

(33) Oh, J. K.; Drumright, R.; Siegwart, D. J.; Matyjaszewski, K. The Development of Microgels/nanogels for Drug Delivery Applications. *Progr. Polym. Sci.* 2008, 33, 448−477.

(34) Saunders, B. R.; Vincent, B. Microgel Particles as Model Colloids: Theory, Properties and Applications. *Adv. Colloid Interface Sci.* 1999, 80, 1−25.

(35) Chen, M.; Mokhtar, M. Z.; Whittaker, E.; Lian, Q.; Hamilton, B.; O'Brien, P.; Zhu, M.; Cui, Z.; Haque, S. A.; Saunders, B. R. Reducing Hole Transporter Use and Increasing Perovskite Solar Cell Stability with Dual-role Polystyrene Microgel Particles. *Nanoscale* 2017, 9, 10126−10137.

(36) Dokkhan, C.; Mokhtar, M. Z.; Chen, Q.; Saunders, B. R.; Hodson, N. W.; Hamilton, B. Using Microgels to Control the Morphology and Optoelectronic Properties of Hybrid Organic−Inorganic Perovskite Films. *Phys. Chem. Chem. Phys.* 2018, 20, 27959−27969.

(37) Crowther, H. M.; Vincent, B. Swelling Behavior of Poly- N-isopropylacrylamide Microgel Particles in Alcoholic Solutions. *Colloid Polym. Sci.* 1998, 276, 46−51.

(38) Zhou, S.; Chu, B. Synthesis and Volume Phase Transition of Poly(methacrylic acid-co-N-isopropylacrylamide) Microgel Particles in Water. *J. Phys. Chem. B* 1998, 102, 1364−1371.

(39) Zhan, Y.; Gonçalves, M.; Yi, P.; Capelo, D.; Zhang, Y.; Rodrigues, J.; Liu, C.; Tomás, H.; Li, Y.; He, P. Thermo/redox/pH-triple Sensitive Poly(N-isopropylacrylamide-co-acrylic acid) Nanogels for Anticancer Drug Delivery. *J. Mater. Chem. B* 2015, 3, 4221−4230.

(40) Zadeh, N. J.; Zarandi, M. B.; Nateghi, M. R. Optical Properties of the Perovskite Films Deposited on Meso-porous TiO2 by One step and Hot Casting Techniques. *Thin Solid Films* 2019, 671, 139−146.

(41) Senff, H.; Richtering, W. Temperature Sensitive Microgel Suspensions: Colloidal Phase Behavior and Rheology of Soft Spheres. *J. Chem. Phys.* **1999**, *111*, 1705−1711.

(42) Bachman, H.; Brown, A. C.; Clarke, K. C.; Dhada, K. S.; Douglas, A.; Hansen, C. E.; Herman, E.; Hyatt, J. S.; Kodlekere, P.; Meng, Z.; Saxena, S.; Spears, M. W., Jr.; Welsch, N.; Lyon, L. A. Ultrasoft, Highly Deformable Microgels. *Soft Matter* **2015**, *11*, 2018−2028.

(43) Krebs, F. C. Fabrication and Processing of Polymer Solar Cells: A Review of Printing and Coating Techniques. *Sol. Energy Mater. Sol. Cells* **2009**, *93*, 394−412.

(44) De Lange, M. F.; Vlugt, T. J. H.; Gascon, J.; Kapteijn, F. Adsorptive Characterization of Porous Solids: Error Analysis Guides the Way. *Microporous Mesoporous Mater.* **2014**, *200*, 199−215.

(45) Hong Pan, J.; In Lee, W. Selective Control of Cubic and Hexagonal Mesophases for Titania and Silica Thin Films with Spin-coating. *New J. Chem.* **2005**, *29*, 841−846.

(46) Fu, Y.; Meng, F.; Rowley, M. B.; Thompson, B. J.; Shearer, M. J.; Ma, D.; Hamers, R. J.; Wright, J. C.; Jin, S. Solution Growth of Single Crystal Methylammonium Lead Halide Perovskite Nanostructures for Optoelectronic and Photovoltaic Applications. *J. Am. Chem. Soc.* **2015**, *137*, 5810−5818.

(47) Umeyama, T.; Imahori, H. A Chemical Approach to Perovskite Solar Cells: Control of Electron-transporting Mesoporous TiO2 and Utilization of Nanocarbon Materials. *Dalton Trans.* **2017**, *46*, 15615−15627.

(48) Adhyaksa, G. W. P.; Brittman, S.; Āboliņš, H.; Lof, A.; Li, X.; Keelor, J. D.; Luo, Y.; Duevski, T.; Heeren, R. M. A.; Ellis, S. R.; Fenning, D. P.; Garnett, E. C. Understanding Detrimental and Beneficial Grain Boundary Effects in Halide Perovskites. *Adv. Mater.* **2018**, *30*, No. 1804792.

(49) Yang, S.; Dai, J.; Yu, Z.; Shao, Y.; Zhou, Y.; Xiao, X.; Zeng, X. C.; Huang, J. Tailoring Passivation Molecular Structures for Extremely Small Open-Circuit Voltage Loss in Perovskite Solar Cells. *J. Am. Chem. Soc.* **2019**, *141*, 5781−5787.

(50) Liu, Z.; Krückemeier, L.; Krogmeier, B.; Klingebiel, B.; Márquez, J. A.; Levcenko, S.; Öz, S.; Mathur, S.; Rau, U.; Unold, T.; Kirchartz, T. Open-Circuit Voltages Exceeding 1.26 V in Planar Methylammonium Lead Iodide Perovskite Solar Cells. *ACS Energy Lett.* **2019**, *4*, 110−117.

(51) Wolff, C. M.; Zu, F.; Paulke, A.; Toro, L. P.; Koch, N.; Neher, D. Reduced Interface-Mediated Recombination for High Open-Circuit Voltages in CH3NH3PbI3 Solar Cells. *Adv. Mater.* **2017**, *29*, No. 1700159.

(52) Snaith, H. J.; Abate, A.; Ball, J. M.; Eperon, G. E.; Leijtens, T.; Noel, N. K.; Stranks, S. D.; Wang, J. T.-W.; Wojciechowski, K.; Zhang, W. Anomalous Hysteresis in Perovskite Solar Cells. *J. Phys. Chem. Lett.* **2014**, *5*, 1511−1515.

(53) Jiang, Q.; Chu, Z.; Wang, P.; Yang, X.; Liu, H.; Wang, Y.; Yin, Z.; Wu, J.; Zhang, X.; You, J. Planar-Structure Perovskite Solar Cells with Efficiency beyond 21%. *Adv. Mater.* **2017**, *29*, No. 1703852.

(54) Seo, J.-Y.; Uchida, R.; Kim, H.-S.; Saygili, Y.; Luo, J.; Moore, C.; Kerrod, J.; Wagstaff, A.; Eklund, M.; McIntyre, R.; Pellet, N.; Zakeeruddin, S. M.; Hagfeldt, A.; Grätzel, M. Boosting the Efficiency of Perovskite Solar Cells with CsBr-Modified Mesoporous TiO2 Beads as Electron-Selective Contact. *Adv. Funct. Mater.* **2018**, *28*, No. 1705763.

(55) Weber, S. A. L.; Hermes, I. M.; Turren-Cruz, S.-H.; Gort, C.; Bergmann, V. W.; Gilson, L.; Hagfeldt, A.; Graetzel, M.; Tress, W.; Berger, R. How the Formation of Interfacial Charge Causes Hysteresis in Perovskite Solar Cells. *Energy Environ. Sci.* **2018**, *11*, 2404−2413.

(56) Bi, C.; Wang, Q.; Shao, Y.; Yuan, Y.; Xiao, Z.; Huang, J. Non-wetting Surface-driven High-aspect-ratio Crystalline Grain Growth for Efficient Hybrid Perovskite Solar Cells. *Nat. Commun.* **2015**, *6*, No. 7747.

(57) Yun, J. S.; Kim, J.; Young, T.; Patterson, R. J.; Kim, D.; Seidel, J.; Lim, S.; Green, M. A.; Huang, S.; Ho-Baillie, A. Humidity-Induced Degradation via Grain Boundaries of HC(NH2)2PbI3 Planar Perovskite Solar Cells. *Adv. Funct. Mater.* **2018**, *28*, No. 1705363.

(58) Wang, Q.; Chen, B.; Liu, Y.; Deng, Y.; Bai, Y.; Dong, Q.; Huang, J. Scaling behavior of Moisture-induced Grain Degradation in Polycrystalline Hybrid Perovskite Thin Films. *Energy Environ. Sci.* **2017**, *10*, 516−522.

(59) Xu, Z.; Liu, Z.; Li, N.; Tang, G.; Zheng, G.; Zhu, C.; Chen, Y.; Wang, L.; Huang, Y.; Li, L.; Zhou, N.; Hong, J.; Chen, Q.; Zhou, H. A Thermodynamically Favored Crystal Orientation in Mixed Formamidinium/Methylammonium Perovskite for Efficient Solar Cells. *Adv. Mater.* **2019**, *31*, No. e1900390.

(60) Xie, L.-Q.; Chen, L.; Nan, Z.-A.; Lin, H.-X.; Wang, T.; Zhan, D.-P.; Yan, J.-W.; Mao, B.-W.; Tian, Z.-Q. Understanding the Cubic Phase Stabilization and Crystallization Kinetics in Mixed Cations and Halides Perovskite Single Crystals. *J. Am. Chem. Soc.* **2017**, *139*, 3320−3323.

(61) Pascoe, A. R.; Yang, M.; Kopidakis, N.; Zhu, K.; Reese, M. O.; Rumbles, G.; Fekete, M.; Duffy, N. W.; Cheng, Y.-B. Planar Versus Mesoscopic Perovskite Microstructures: The Influence of CH3NH3PbI3 Morphology on Charge Transport and Recombination Dynamics. *Nano Energy* **2016**, *22*, 439−452.

(62) Reid, O. G.; Yang, M.; Kopidakis, N.; Zhu, K.; Rumbles, G. Grain-Size-Limited Mobility in Methylammonium Lead Iodide Perovskite Thin Films. *ACS Energy Lett.* **2016**, *1*, 561−565.

(63) Ye, T.; Ma, S.; Jiang, X.; Petrovic, M.; Vijila, C.; Ramakrishna, S.; Wei, L. Electrosprayed TiO2 Nanoporous Hemispheres for Enhanced Electron Transport and Device Performance of Formamidinium Based Perovskite Solar Cells. *Nanoscale* **2017**, *9*, 412−420.

(64) Abdelraouf, O. A. M.; Allam, N. K. Towards Nanostructured Perovskite Solar Cells with Enhanced Efficiency: Coupled Optical and Electrical Modeling. *Sol. Energy* **2016**, *137*, 364−370.

(65) Ameri, M.; Mohajerani, E.; Ghafarkani, M.; Safari, N.; Alavi, S. A. The Investigation of the Unseen Interrelationship of Grain Size, Ionic Defects, Device Physics and Performance of Perovskite Solar Cells. *J. Phys. D: Appl. Phys.* **2019**, *52*, No. 125501.

(66) Bisquert, J.; Mora-Sero, I.; Fabregat-Santiago, F. Diffusion−Recombination Impedance Model for Solar Cells with Disorder and Nonlinear Recombination. *ChemElectroChem* **2014**, *1*, 289−296.

(67) Bag, M.; Renna, L. A.; Adhikari, R. Y.; Karak, S.; Liu, F.; Lahti, P. M.; Russell, T. P.; Tuominen, M. T.; Venkataraman, D. Kinetics of Ion Transport in Perovskite Active Layers and Its Implications for Active Layer Stability. *J. Am. Chem. Soc.* **2015**, *137*, 13130−13137.

(68) Shao, S.; Abdu-Aguye, M.; Sherkar, T. S.; Fang, H.-H.; Adjokatse, S.; Brink, G.; Kooi, B. J.; Koster, L. J. A.; Loi, M. A. The Effect of the Microstructure on Trap-Assisted Recombination and Light Soaking Phenomenon in Hybrid Perovskite Solar Cells. *Adv. Funct. Mater.* **2016**, *26*, 8094−8102.

(69) Chen, X.; Shirai, Y.; Yanagida, M.; Miyano, K. Effect of Light and Voltage on Electrochemical Impedance Spectroscopy of Perovskite Solar Cells: An Empirical Approach Based on Modified Randles Circuit. *J. Phys. Chem. C* **2019**, *123*, 3968−3978.

(70) Zhao, Y.; Nardes, A. M.; Zhu, K. Effective hole extraction using MoOx-Al Contact in Perovskite CH3NH3PbI3 Solar Cells. *Appl. Phys. Lett.* **2014**, *104*, No. 213906.

(71) Liu, C.; Wang, K.; Yi, C.; Shi, X.; Smith, A. W.; Gong, X.; Heeger, A. J. Efficient Perovskite Hybrid Photovoltaics via Alcohol-Vapor Annealing Treatment. *Adv. Funct. Mater.* **2016**, *26*, 101−110.

(72) Yang, Y.; Yan, Y.; Yang, M.; Choi, S.; Zhu, K.; Luther, J. M.; Beard, M. C. Low surface Recombination Velocity in Solution-grown CH3NH3PbBr3 Perovskite Single Crystal. *Nat. Commun.* **2015**, *6*, No. 7961.

(73) Cui, P.; Wei, D.; Ji, J.; Huang, H.; Jia, E.; Dou, S.; Wang, T.; Wang, W.; Li, M. Planar p−n Homojunction Perovskite Solar Cells with Efficiency Exceeding 21.3%. *Nat. Energy* **2019**, *4*, 150−159.

(74) Hellmann, T.; Wussler, M.; Das, C.; Dachauer, R.; El-Helaly, I.; Mortan, C.; Mayer, T.; Jaegermann, W. The Difference in Electronic Structure of MAPI and MASI Perovskites and its Effect on the Interface Alignment to the HTMs spiro-MeOTAD and CuI. *J. Mater. Chem. C* **2019**, *7*, 5324−5332.

(75) Lin, B.-T.; Chen, Y.-F.; Lin, J.-J.; Wu, C.-Y. Temperature Dependence of Resistance and Thermopower of Thin Indium Tin Oxide Films. *Thin Solid Films* **2010**, *518*, 6997−7001.

(76) Li, F.; Chen, C.; Tan, F.; Li, C.; Yue, G.; Shen, L.; Zhang, W. Semitransparent Inverted Polymer Solar Cells Employing a Sol-gel-derived TiO2 Electron-selective Layer on FTO and MoO3/Ag/MoO3 Transparent Electrode. *Nanoscale Res. Lett.* **2014**, *9*, 579.